Received June 19, 2024; accepted September 30, 2024; Date of publication October 08, 2024.
The review of this paper was arranged by Associate Editor Edivan L. C. da Silva and Editor-in-Chief Telles B. Lazzarin.

Digital Object Identifier http://doi.org/10.18618/REP.e202437

Zero Sequence Injection in Delta-CHB STATCOM: Towards Optimum Silicon Area Through Typical Power IGBT/diode Model

Dayane do Carmo Mendonça[1], João Victor Guimarães França[2], Heverton Augusto Pereira[3], Seleme Isaac Seleme Júnior[4], Allan Fagner Cupertino[5]

[1]Federal University of Minas Gerais, Graduate Program in Electrical Engineering, Belo Horizonte, MG, Brazil.
[2]Federal Center of Technological Education of Minas Gerais, Graduate Program in Electrical Engineering, Belo Horizonte, MG, Brazil.
[3]Federal University of Viçosa, Department of Electrical Engineering, Viçosa, MG, Brazil.
[4]Federal University of Minas Gerais, Department of Electronic Engineering, Belo Horizonte, MG, Brazil.
[5]Federal University of Juiz de Fora, Department of Electrical Energy, Juiz de Fora, MG, Brazil.

e-mail: dayane.carmo.mend@gmail.com; joao.v.franca@ufv.br; heverton.pereira@ufv.br; selemejr@gmail.com; allan.cupertino@ufjf.br.

ABSTRACT This work quantifies the impact of third harmonic circulating current injection (THCCI) in a Cascaded H-bridge converter in delta configuration (Delta-CHB) for Static Synchronous Compensator (STATCOM) application. The analyses consist of evaluating the impact of THCCI on the silicon area of semiconductor devices. To achieve this objective, this work develops a typical IGBT/Diode model to determine the nominal current of the devices for a given maximum junction temperature. Commercial devices in the voltage classes of 1700 V, 3300 V, 4500 V, and 6500 V were considered, with nominal currents ranging from 150 A to 3600 A. A hybrid approach based on physical-oriented scaling laws and black-box modeling allows to reach a coefficient of determination higher than 79% for all modeled variables. The results showed an increase of 43.8% in the active area of the IGBT and 30.87% in the active area of the diode when the peak cluster current increased by 62% due to THCCI.

KEYWORDS Delta-CHB, STATCOM, third harmonic, silicon area.

I. INTRODUCTION

A cascaded H-bridge converter in delta configuration (Delta-CHB) is a widespread topology for the Static Synchronous Compensator (STATCOM) market [1]–[3]. A significant drawback of this topology is the capacitor volume and costs due to the presence of low-frequency ripple in the submodule voltage [4], [5].

Recently, the third harmonic circulating current injection (THCCI) was investigated [6], leading to a capacitance reduction of around 17.2%. However, injecting the third harmonic increases power losses and temperatures of semiconductor devices. This phenomenon can be resolved by improving the heat transfer mechanism (heatsink design or cooling) or by increasing the silicon area of the semiconductor devices.

Therefore, this work aims to evaluate the increase in the silicon area of semiconductor devices with THCCI. Looking at this objective, this work proposes a typical IGBT/Diode model to calculate the power losses of semiconductor devices and determine the nominal current of these devices to maintain the same junction temperature.

In this sense, reference [7] was one of the first silicon area optimization works. The approach is to determine the total semiconductor chip area based on the converter operating point and the optimal partitioning of the transistor and diode chip areas. For this, the authors use finite elements and information from the chip area of semiconductor devices. However, chip area information is sometimes not presented in the module datasheets (IGBT+diode). Reference [8] developed a model to generalize the conduction and switching losses of IGBT modules using a semiconductors physics-oriented model. However, the model considered few semiconductors per studied voltage range. In addition, corrections for power losses as a function of operating current were not considered. Thus, this work presents a model based on several semiconductor devices with different blocking voltages and considers other operating ranges, different from the nominal current value. In this way, the typical IGBT/Diode model is used, allowing silicon area optimization.

This paper is an extended version of [9] and presents the typical IGBT/diode model as a function of blocking voltage, which was not performed in the previous publication. A hybrid approach based on physical-oriented scaling laws and black-box modeling (curve fitting) is employed. Furthermore, a comparison between the typical model and real device data was performed for validation. Then, the effective increase in silicon area caused by THCCI is derived. The rest of this paper is outlined as follows. Section II presents the methodology used for silicon area optimization. Section III presents the validation of the typical IGBT/Diode model and Section IV shows the results of the active area of semiconductor devices. Finally, the conclusions are stated in Section VII.

II. METHODOLOGY

A. DELTA-CHB WITH THIRD HARMONIC CIRCULATING CURRENT INJECTION

The schematic of Delta-CHB-based STATCOM is illustrated in Fig. 1. As observed, the Delta-CHB presents a path for zero sequence current flow, which theoretically does not affect the output currents (grid current). The computation of zero sequence can be used for capacitor voltage balancing and for capacitor voltage ripple reduction.

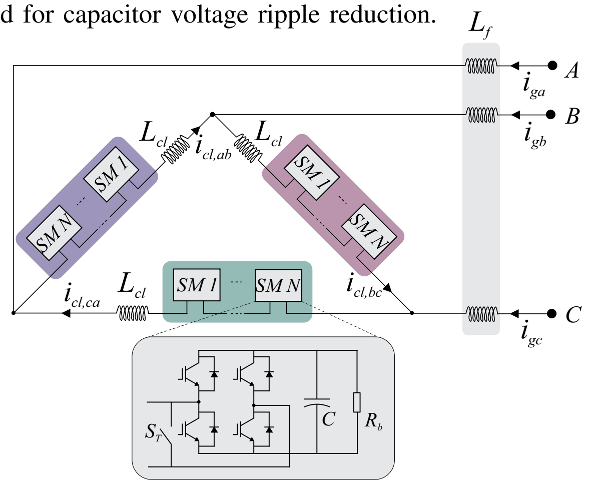

FIGURE 1. Schematic of the Delta-CHB based STATCOM. The submodule is a full-bridge converter.

The control strategy used in this work (Fig. 2) is the same adopted in references [4], [10], which is a classical control strategy for Delta-CHB converters. Circulating current (zero-sequence current) is used to exchange energy among the converter clusters and to reach capacitor voltage balancing. The circulating current reference is calculated by the cluster voltage balancing control. Furthermore, the output current control is performed in a synchronous reference frame (dq). The direct axis current reference is calculated by the global voltage control, which computes the energy exchanged between the converter and the grid to charge/discharge the submodule capacitors. Finally, the quadrature axis current reference is calculated by the reactive power control loop. In the current loops, only controllers with proportional gain were used, considering the presence of integral action in the external loops (global voltage control and reactive power control).

The global voltage control calculates the active power required from the grid to supply the converter energy losses. The control is performed based on the average of the sum of the capacitor voltages in the clusters. On the other hand, the reactive power control calculates the quadrature axis current reference to be injected into the grid.

The cluster balancing control is responsible for exchanging energy among the converter clusters without affecting the output current. This control calculates the fundamental circulating current reference, which is in phase with the line-to-line grid voltage, to drain/supply active power for the cluster that has the highest/lower voltage. In addition, the THCCI is added to the cluster balance control output.

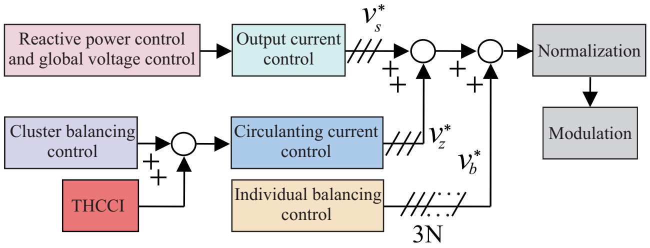

FIGURE 2. Overview of the Delta-CHB control strategy.

The three-phase references (v_s^* and v_z^*) are summed and then added together with the voltage v_z^*, which is different for each submodule. Then the signal is normalized by the sum of the capacitor voltage and goes to the modulator.

The THCCI is investigated in [6], where an analytical model of the voltage ripple of the capacitors is presented (Eq. (1)). In addition, the optimum third harmonic amplitude and angle (for capacitor voltage reduction) are computed.

$$\begin{aligned} v_c^{\Sigma} = V_{dc} + & \frac{N\widehat{V}\widehat{I}}{4\omega C V_{dc}} \sin\left(2\omega t + 2\theta_v + \delta + \varphi + \frac{\pi}{3}\right) + \\ & \frac{N\widehat{V}\widehat{I}_{th}}{4\omega C V_{dc}} \sin\left(2\omega t + 2\theta_v - \delta + \varphi_{th} - \frac{\pi}{6}\right) + \\ & \frac{N\widehat{V}\widehat{I}_{th}}{8\omega C V_{dc}} \sin\left(4\omega t + 4\theta_v + \delta + \varphi_{th} + \frac{\pi}{6}\right) + \\ & \frac{N\widehat{V}_{th}\widehat{I}}{4\omega C V_{dc}} \sin\left(2\omega t + 2\theta_v + \delta_{th} - \varphi - \frac{\pi}{6}\right) + \\ & \frac{N\widehat{V}_{th}\widehat{I}}{8\omega C V_{dc}} \sin\left(4\omega t + 4\theta_v + \delta_{th} + \varphi + \frac{\pi}{6}\right) + \\ & \frac{N\widehat{V}_{th}\widehat{I}_{th}}{12\omega C V_{dc}} \sin\left(6\omega t + 6\theta_v + \delta_{th} + \varphi_{th}\right), \end{aligned} \tag{1}$$

where $\widehat{V}$ is the output voltage (line-to-neutral) required for grid connected applications and $\widehat{I}$ is the fundamental grid current. V_{dc} is the average of the sum of capacitors voltage. $\widehat{V}_{th}$ and $\widehat{I}_{th}$ are the third harmonic voltage and current. ω is the grid frequency in rad/s. δ and δ_{th} are the angles of the fundamental and third harmonic voltage. φ and φ_{th} are the angles of the fundamental and third harmonic current. θ_v assumes the values $\left(0, \frac{-2\pi}{3}, \frac{2\pi}{3}\right)$, depending on the phase.

Figure 4 presents the experimental results of the THCCI for a small-scale prototype. The parameters are presented in Tab. 1 and the experimental setup in Fig. 3. From the capacitor voltage, it is possible to observe in a reduction in the 2nd harmonic component (from 1.525 V to 0.3192 V) and an increase in the 4th harmonic component (from 0.08775 V to 0.2287 V). In these results, the converter operates in an inductive region, with 6 A of fundamental grid current and 2 A of third harmonic current (peak values). In addition, the third harmonic current was injected in phase with the fundamental component of the cluster current.

TABLE 1. Parameters of the converter (simulation and experimental setup).

Parameter	Simulation	Experimental
Line-to-line RMS grid voltage (V_g)	13.8 kV	57.56 V
Effective dc-link voltage (V_{dc})	21.58 kV	144 V
Nominal power (S_n)	17 Mvar	423 var
Transformer inductance (L_f)	4.75 mH	-
Transformer X/R ratio	18	-
Cluster inductance (L_{cl})	5 mH	5.5 mH
Cluster inductor X/R ratio	17	16
Cell capacitance (C)	4.172 mF	680 μF
Nominal cell voltage (v^*_{cell})	899.17 V	48 V
Grid frequency (f_g)	60 Hz	60 Hz
Switching frequency (f_{sw})	270 Hz	1.5 kHz
Sampling frequency (f_s)	12.96 kHz	9 kHz
Number of cells (N)	24 per cluster	3 per cluster

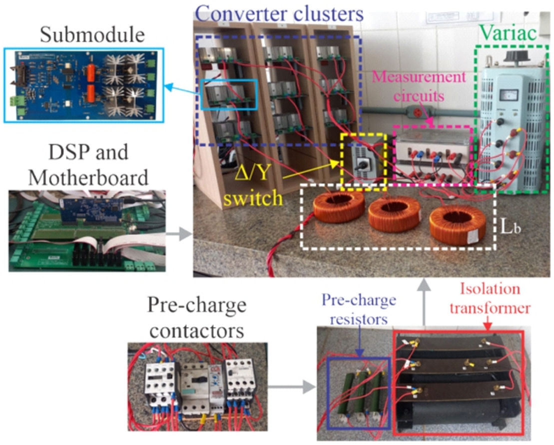

FIGURE 3. Experimental setup. *Remark:* Obtained from [11].

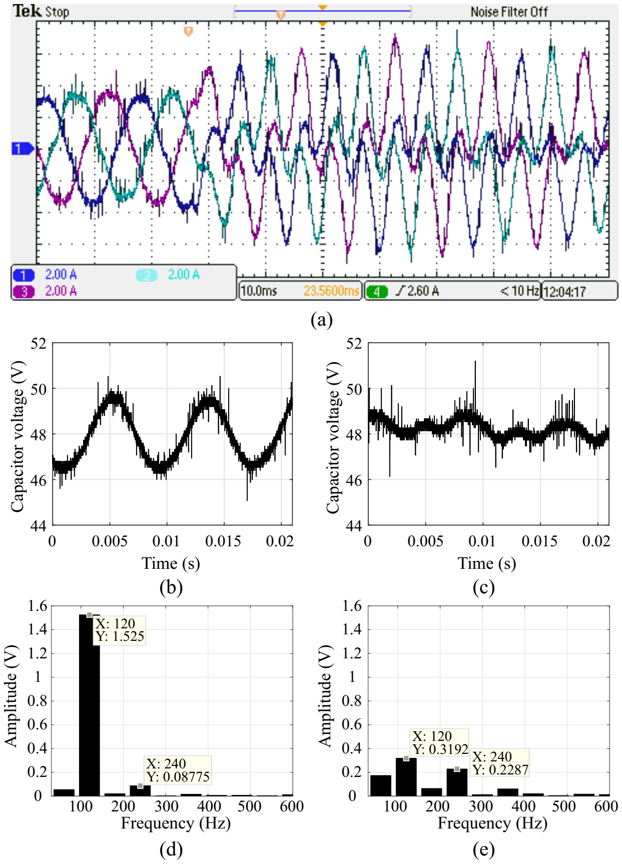

(a)

(b) (c)

(d) (e)

FIGURE 4. Small-scale prototype results: (a) Cluster currents (i_{cl}); (b) Submodule voltage without THCCI; (c) Submodule voltage with THCCI; (d) Submodule voltage spectrum without THCCI; (e) Submodule voltage spectrum with THCCI. Note: The dc component was suppressed from the voltage spectrum for better visualization of the other frequencies.

B. SILICON AREA OPTIMIZATION

As shown in Fig. 4a, the THCCI increases the cluster current rms value, increasing the semiconductor device temperature. In this case, the silicon area should be increased. The flowchart shown in Fig. 5 is used to compute the minimum silicon area for a given junction temperature and heatsink parameters. First, an initial value of the nominal current of the semiconductor devices is defined and then, the power losses and junction temperature are calculated based on the chosen heatsink data and the loss curves obtained by the typical IGBT/Diode model. If the junction temperature is equal to the set temperature, the process stops. Otherwise, the nominal current value is increased and the process repeats. In this process, this work assumes independent heatsinks for each submodule. Also, the four IGBTs and four diodes share the same heatsink, which is a common approach in commercial systems. Therefore, changing the nominal current of IGBT affects the temperature of the diodes and vice versa. The thermal equivalent circuit model to obtain the average junction temperature of the devices is presented in Fig. 6. The junction temperature of the IGBTs and diodes is calculated considering the average of the four devices.

III. TYPICAL IGBT/DIODE MODEL

Commercial tools that estimate power losses in semiconductor devices usually employ, at least, the following data: IGBT on-state voltage drop, diode voltage drop, IGBT turn-on and turn-off energies, diode reverse recovery energy. For a more accurate estimation, thermal dependence is important, and data at different temperatures should be used. Also, the IGBT and diode thermal impedances should be known [12], [13]. This data set can be usually obtained in the manufacturer datasheet. In this paper, a typical IGBT/diode model is developed to obtain this information for a given rated voltage and rated current. This section presents this model considering data normalization and using physics-oriented scaling laws. The method is derived with some examples. The other data related to the typical model are presented in the Appendix.

ABB modules with blocking voltages of 1700 V, 3300 V, 4500 V, and 6500 V were considered to model typical IGBTs and diodes, as presented in Tables 2, 3, 4 and 5

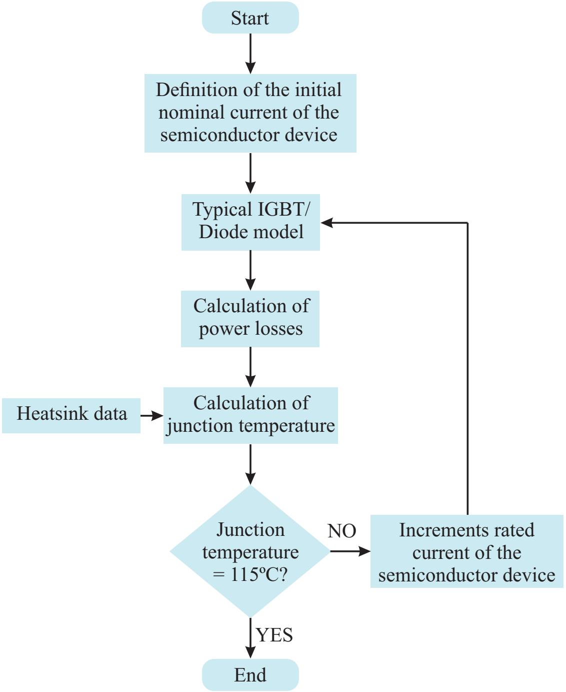

FIGURE 5. Silicon area optimization flowchart.

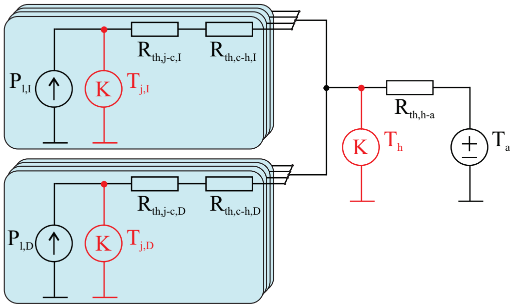

FIGURE 6. Thermal equivalent circuit model to obtain the average junction temperature of the devices.

in the appendix. This manufacturer was selected due to the higher number of available information for medium voltage IGBTs and diodes. In total, 41 devices were considered as a database. In the analysis of conduction and switching losses, three effects were considered:

1) The variation of the collector-emitter voltage (V_{ce}), the turn-on switching energy (E_{on}) and the turn-off switching energy (E_{off}) with the operating condition, i. e., the operating current of the semiconductor device;
2) Nominal value of V_{ce}, E_{on} and E_{off}, i.e. the value at the nominal current;
3) The variation of V_{ce}, E_{on} and E_{off} with the blocking voltage of the semiconductor device.

A. CONDUCTION LOSSES

Figure 7 shows the per-unit collector-emitter voltage (V_{ce}) versus collector current (I_c) of ABB IGBTs at 25°C. The base current is the nominal current of the device, while the base voltage corresponds to the voltage drop at the nominal current. Through the datasheet of the semiconductor devices, a curve fitting was performed.

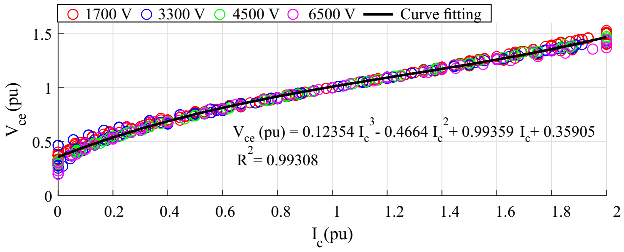

FIGURE 7. Curve fitting of typical IGBT conduction losses for 25°C in pu values.

Fig. 8(a) shows the device conductance at a nominal collector current with the datasheet information. As observed, the conductance decreases with the increase in blocking voltage, and consequently the voltage V_{ce} decreases, for the same nominal current value. The correction concerning the blocking voltage was carried out considering a constant loss density, i.e., a constant value of losses per square meter, as described in [14]. Accordingly,

$$\frac{P}{S}\left(\frac{W}{m^2}\right) = \frac{RI^2}{S}, \tag{2}$$

where P is the power and S is the area of the semiconductor devices. R is the equivalent electrical resistance and I is the operation current. Considering two devices with the same power loss density, the following relationship is obtained:

$$\frac{P_1}{S_1} = \frac{\rho l_1 I^2}{S_1^2} = \frac{P_2}{S_2} = \frac{\rho l_2 I^2}{S_2^2}, \tag{3}$$

where ρ is the material resistivity and l_1 and l_2 are the chip lengths. The following equation is derived from (3).

$$\frac{S_1}{S_2} = \sqrt{\frac{l_1}{l_2}} \propto \sqrt{\frac{V_{B1}}{V_{B2}}}, \tag{4}$$

where V_{B1} and V_{B2} represent the blocking voltages of the devices.

The relationship between the devices conductances with different blocking voltages can be obtained through the following analysis.

$$\frac{G_2}{G_1} = \frac{\frac{S_2}{\rho l_2}}{\frac{S_1}{\rho l_1}} = \frac{S_2}{S_1}\frac{l_1}{l_2} \propto \sqrt{\frac{V_{B2}}{V_{B1}}}\frac{V_{B1}}{V_{B2}} \propto \sqrt{\frac{V_{B1}}{V_{B2}}}. \tag{5}$$

Fig. 8(b) shows the device conductance at a nominal collector current with blocking voltage correction. In this case, all devices are on 1700 V base. Then, the performed curve fitting at 25°C is obtained. Therefore, the voltage V_{ce} is the combination of the polynomials obtained by the two curve fittings: V_{ce}=$V_{ce}(\text{pu}).V_{ce,n}(\text{V})$. To obtain $V_{ce,n}$ for other blocking voltage values, the relationship obtained in (6) must be used, as follows:

$$V_{ce,n} = V'_{ce}\sqrt{\frac{V_{B2}}{1700}}, \tag{6}$$

where V'_{ce} is the collector-emitter voltage at 1700 V, for the curve fitting obtained in Fig. 8(b).

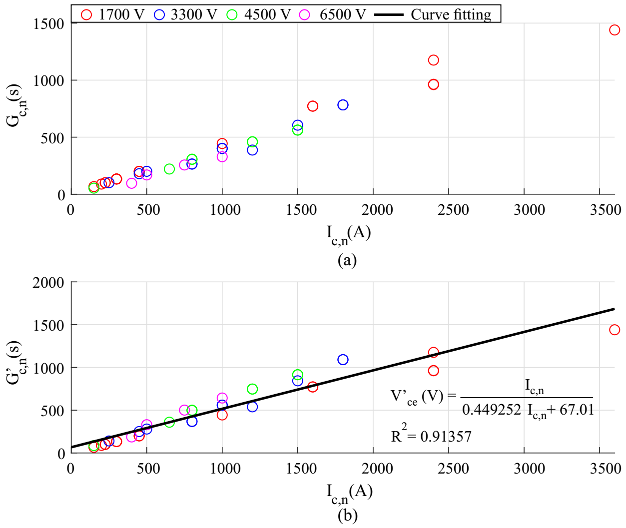

FIGURE 8. Typical IGBT conduction losses for 25°C in nominal values: (a) without blocking voltage correction; (b) with blocking voltage correction and curve fitting.

The curve fitting obtained for IGBT at 125°C is presented in the appendix (Figs. 21 and 22). The same procedure is adopted for diode[1]. The results are presented in Figs. 27, 28, 31 and 32 for 25°C and 125°C.

B. SWITCHING LOSSES

Figure 9 shows the turn-on switching energy (E_{on}) versus collector current (I_c) of ABB IGBTs at 25°C. The base current is the nominal current of the device and the base energy is the turn-on energy at nominal current. Through the datasheet of the semiconductor devices, a curve fitting was performed.

Fig. 10(a) shows the graph of turn-on switching energy in the nominal condition versus the nominal collector current with the datasheet information. As observed, the energy losses increase with the increase in blocking voltage, for the same nominal current value. According to [8], the switching energies are expected to scale with the square of the blocking voltage. Therefore, Fig. 10(b) shows the device turn-on energy at a nominal collector current with blocking voltage correction (all devices are on 1700 V base), and the curve fitting is performed at 25°C.

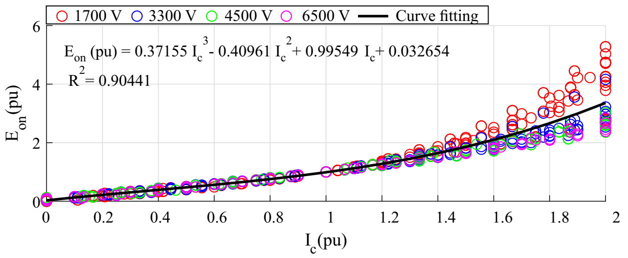

FIGURE 9. Curve fitting of IGBT turn-on energy for 25°C in pu values. Note: The observed scattering is associated with the difficulty of measuring switching losses and the great influence of parasitic elements, especially at high currents.

In addition, the turn-on switching energy E_{on} is the combination of the polynomials obtained by the two curve fittings: $E_{on}{=}E_{on}(\mathrm{pu}).E_{on,n}(\mathrm{J})$. To obtain $E_{on,n}$ for other blocking voltage values, the following relationship should be used:

$$E_{on,n} = E'_{on,n}\frac{V_{B2}^2}{1700^2}, \tag{7}$$

where $E'_{on,n}$ is the turn-on energy at 1700 V, for the curve fitting obtained in Fig. 10(b).

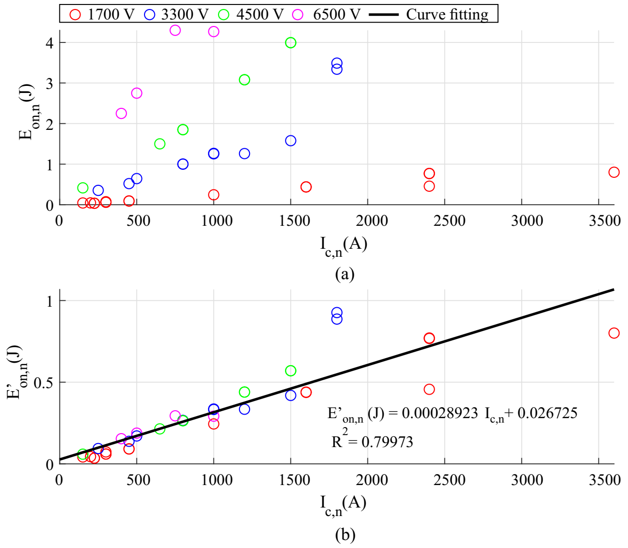

FIGURE 10. Typical IGBT turn-on energy for 25°C in nominal values: (a) without blocking voltage correction; (b) with blocking voltage correction and curve fitting.

The curve fitting obtained for IGBT at 125°C is presented in the appendix (Figs. 23 and 24). The same reasoning can be done for the turn-off switching energy, as presented in the appendix (Figs. 19 and 20 at 25°C and Figs. 25 and 26 at 125°C). The appendix also presents the curve fitting of reverse recovery energy for diodes, where the same approach is used (Figs. 29 and 30 at 25°C and Figs. 33 and 34 at 125°C).

---

[1] The same nominal current was assumed for the diode, in the sense that they are combined in the same encapsulation. However, it is common to find modules on the market with diodes with an area smaller than the IGBT, considering that commercial power modules are generally optimized for application in motor drive inverters, where the loading of the diodes is expected to be lower. It should be highlighted that this does not hold for STATCOM applications.

C. THERMAL RESISTANCES

To accurately calculate the power losses in semiconductor devices, the junction-to-case and case-heatsink thermal resistances should be known. Also, this variable is usually an important reliability metric. Fig. 11 shows the graph of junction-to-case thermal conductance versus the switched power ($V_B I_{c,n}$) of select IGBTs and the curve fitting performed. Conductance was considered by the linear relationship with the switching power of the semiconductor device, similar to reference [8].

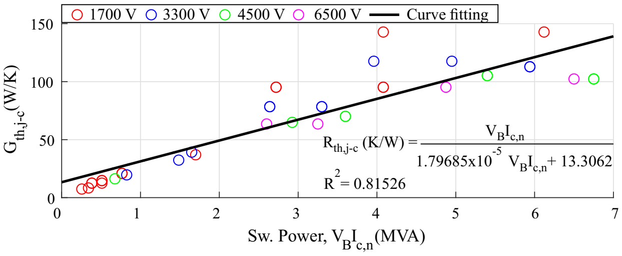

FIGURE 11. Curve fitting of typical IGBT junction-to-case thermal resistance. The relationship between blocking voltage and nominal current is already in the curve fitting equation itself.

The same analysis can be done with the case-heatsink thermal conductance and for diodes thermal conductances, as presented in the appendix (Figs. 35, 36 and 37). It is worth mentioning that the analysis presented in this paper focuses on steady-state temperature. Therefore, the typical model does not consider the thermal capacitances. This can be done in further publications and the reader can find inspiration in [15].

IV. TYPICAL IGBT/DIODE MODEL VALIDATION

The typical IGBT/Diode model was validated for the Delta-CHB STATCOM simulation, with the parameters in Table 1. For this analysis, devices with 1700 V blocking voltage were considered. The following part numbers were analyzed: 5SNG 0450R170390, 5SND 0800M170100 and 5SNA 1600N170300. A heatsink-to-ambient thermal resistance of 0.0536 $\frac{K}{W}$ and an ambient temperature of 25°C were considered. Furthermore, the STATCOM is operating on 1 pu of capacitive reactive power.

Fig. 12 presents the IGBT junction temperature obtained through the typical model and the real data provided by the manufacturer. The comparison is performed for the scenario without THCCI (Fig. 12(a)) and with THCCI (Fig. 12(b)). The largest error observed was 16.43% for the 1600 A device and with the third harmonic injection.

Fig. 13 presents the diode junction temperature obtained through the typical model and the real data provided by the manufacturer. The comparison is performed for the scenario without THCCI (Fig. 13(a)) and with THCCI (Fig. 13(b)). The largest error observed was 16.25% for the 1600 A device and with the third harmonic injection.

The interesting thing about analyzing the junction temperature is that includes the combined effects of conduction losses, switching losses and thermal impedances. However, an analysis of the conduction and switching losses was performed separately for IGBT and diode for the scenario without THCCI.

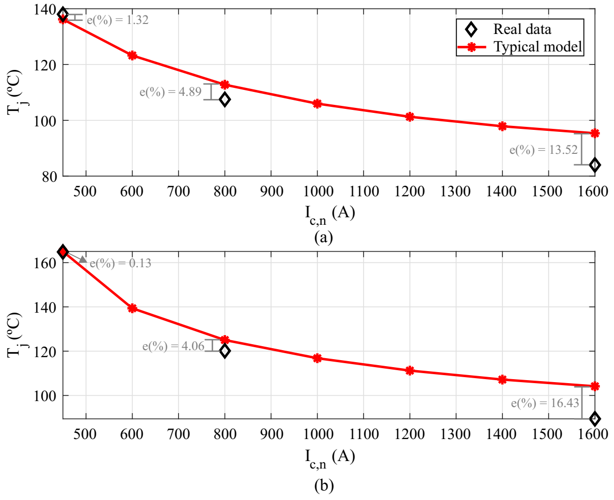

FIGURE 12. Junction temperature comparison between typical model and real data for IGBT (a) without THCCI and (b) with THCCI.

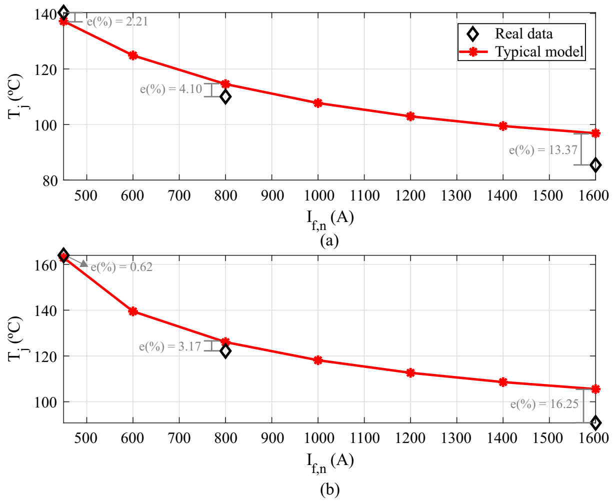

FIGURE 13. Junction temperature comparison between typical model and real data for diode (a) without THCCI and (b) with THCCI.

Fig. 14 presents the IGBT conduction losses obtained through the typical model and the real data provided by the manufacturer (Fig. 14(a) for IGBT and Fig. 15(b) for diode). The largest error observed was 9.82% for 1600 A IGBT. The conduction losses presented small errors that are justified by the characteristics of the data and the coefficient of determination obtained in the curve fitting.

Fig. 15 presents the IGBT switching losses obtained through the typical model and the real data provided by the manufacturer (Fig. 15(a) for IGBT and Fig. 15(b) for diode). The largest error observed was 95.44% for 1600 A diode. The switching losses presented larger errors due to the data characteristics. The switching energy data presents a certain

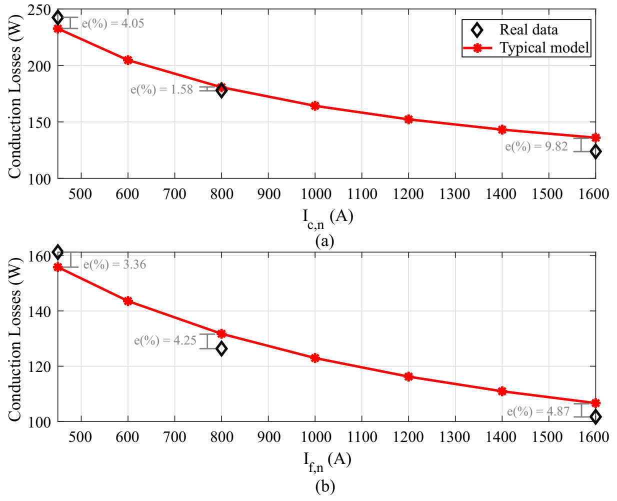

FIGURE 14. Conduction losses comparison between typical model and real data for (a) IGBT and (b) diode.

spread, being smaller around 1 pu. Therefore, the 450 A and 1600 A devices will present larger errors compared to the 800 A device. Furthermore, by analyzing the nominal energy data, it is possible to verify a greater spread that is reflected in the coefficient of determination of the curve fitting performed. It is worth mentioning that delta-CHB topology usually employs low switching frequencies. In this case, the effect of conduction losses is dominant in the heat generation in the power device. For this reason, although the errors in switching losses are quite high, the junction temperature is reasonably estimated.

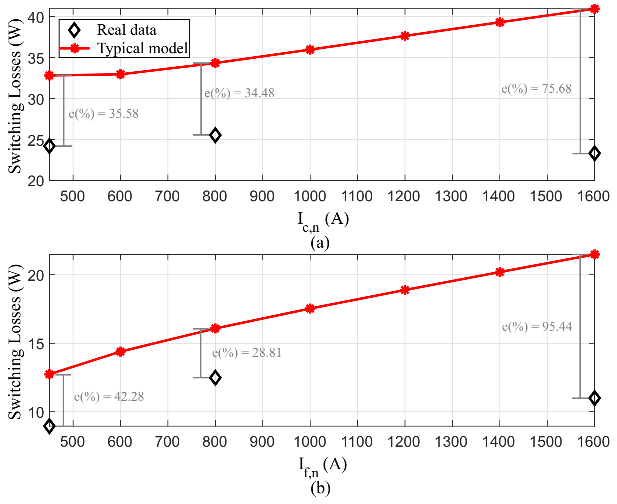

FIGURE 15. Switching losses comparison between typical model and real data for (a) IGBT and (b) diode.

V. RESULTS

As shown in Fig. 5, the objective is to determine the nominal current that the semiconductor device needs to meet the junction temperature requirement.

Thus, Fig. 16 shows how the device junction temperature varies when changing the nominal current of the diode ($I_{f,n}$) and the nominal current of the IGBT ($I_{c,n}$). Therefore, one surface is obtained for the diode and another for the IGBT. The intersection between the two surfaces indicates when the junction temperature is equal for both devices. As observed, this analysis allows us to go beyond the devices commercially available, allowing us to employ a combination of IGBT and diode chips with different rated currents. The dot indicates the desired temperature of 115°C. Fig. 16(a) presents this result without THCCI and Fig. 16(b) with THCCI. As expected, the third harmonic injection increases the junction temperature of the devices. Furthermore, the diode requires a higher nominal current than the IGBT to operate at the same temperature. This is common for the studied application, where the diodes present relatively high current efforts due to reactive power processing.

To compute the silicon area, a curve fitting that relates the silicon area with the nominal current was obtained. Reference [16] shows the estimated total die area installed within Si IGBT packages versus the rated current for blocking voltages of 1700 V, 3300 V, and 4500 V. This reference considers the total area of the chip. Therefore, the curve fitting returns a larger area for the same nominal current value, when compared to the model proposed in this paper. Furthermore, the authors do not mention where the IGBT data were taken from.

Reference [17] chose the Infineon Trench and Field Stop series 1200 V IGBT4 and 600 V IGBT3 as the database. A curve fitting was carried out considering the data provided by the manufacturers for IGBTs and diodes in the 600 V and 1200 V voltage classes. However, analyzing the data, it is clear that the authors also looked at the total area of the chip, i.e. including gate and chip passivation area.

However, the analysis carried out in this paper focuses on the active area (emitter), i.e., discounting the gate area in the case of IGBT. For this, ABB dies for 1700 V were used (Tab. 6 for IGBT and Tab. 7 for diode, see appendix). Fig. 17 presents the result for the IGBT (same can be done for the diode, as presented in Fig. 38 in appendix). Data for other voltage classes are not provided by the manufacturer, but the relationship obtained in (4) can be used to obtain the active area of devices for another voltage class. This relationship was used in data from reference [17] and a coefficient of determination above 94% was obtained for the diode and IGBT curve fitting.

Finally, Fig. 18 shows the increase in the silicon area of semiconductor devices with the third harmonic injection. Although the optimum THCCI increases the peak cluster current in 62%, the maximum increase in the semiconductor area is 43.8% for the diode.

VI. CONCLUSION

The third harmonic circulating current injection reduces the voltage ripple and consequently the required capacitance

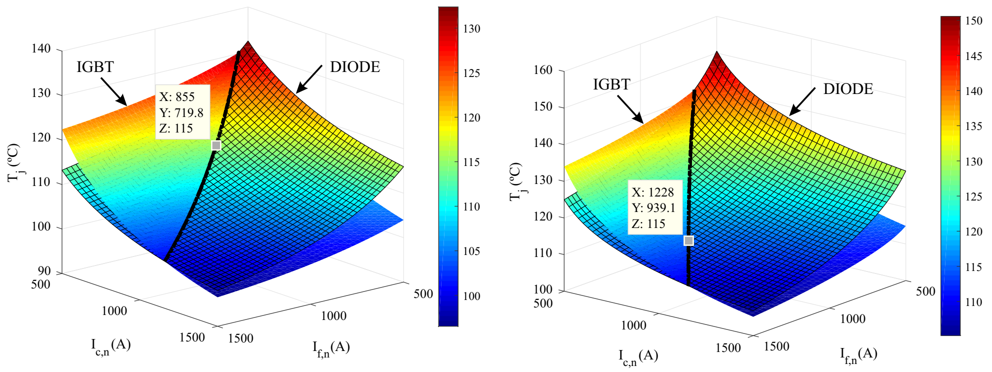

(a) (b)

FIGURE 16. Junction temperature of semiconductor devices as a function of their nominal currents when the STATCOM exchanges 17 Mvar with the grid.

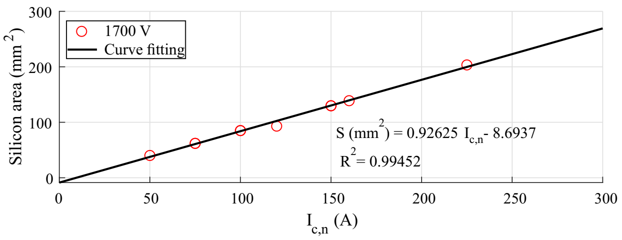

FIGURE 17. Curve fitting of typical silicon area for IGBT.

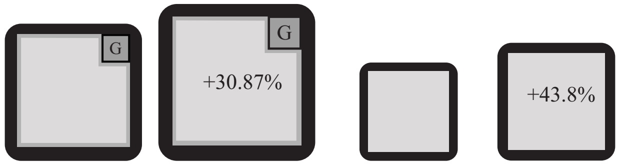

S_I = 658.02 mm^2 S_I = 861.15 mm^2 S_D = 386.88 mm^2 S_D = 556.21 mm^2

(a) (b) (c) (d)

FIGURE 18. Active area of (a) IGBT (without THCCI); (b) IGBT (with THCCI); (c) Diode (without THCCI); (d) Diode (with THCCI). Note: This draw is presented in scale.

value. However, injecting the third harmonic increases power losses and temperatures of semi- conductor devices. This phenomenon can be resolved by increasing the silicon area of the semiconductor devices.

Therefore, this work presented a methodology to determine the increase in the silicon area of semiconductor devices when injecting a third harmonic current in Delta-CHB STATCOM. This method is based on a typical IGBT and diode model which is obtained through curve fitting with data available in the manufacturer's datasheet. The typical IGBT model led to a coefficient of determination higher than 79% obtained for all modeled variables.

The results showed an increase of 30.87% in the active area of the IGBT and 43.8% in the active area of the diode when the peak cluster current increased by 62% in the third harmonic circulating injection.

Finally, the typical IGBT/diode model can be derived using data from other manufacturers or characterization data. It should be highlighted that the accuracy of temperature estimation will depend on the quality and accuracy of the data provided as inputs.

APPENDIX

A. Curve fitting for IGBT and diodes power losses

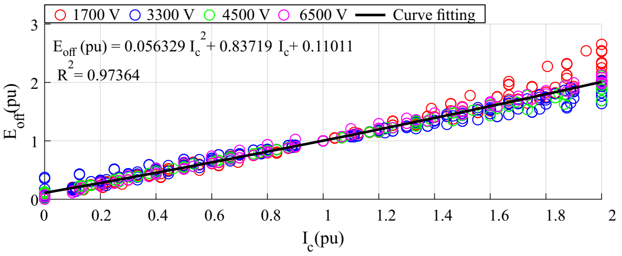

FIGURE 19. Curve fitting of typical IGBT turn-off energy for 25°C in pu values.

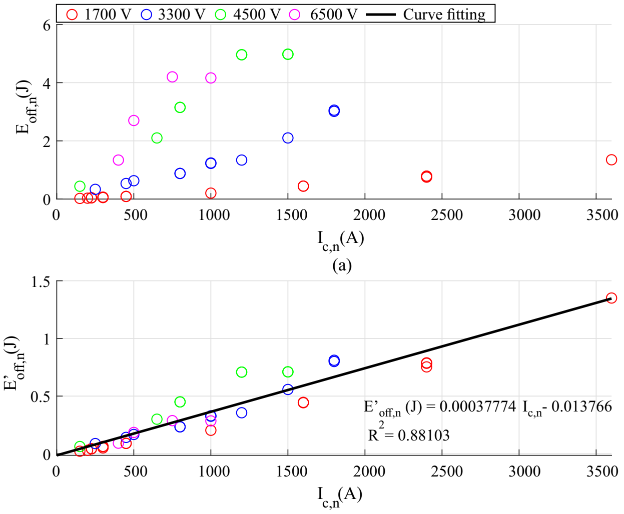

(a)

(b)

FIGURE 20. Typical IGBT turn-off energy for 25°C in nominal values: (a) without blocking voltage correction; (b) with blocking voltage correction and curve fitting.

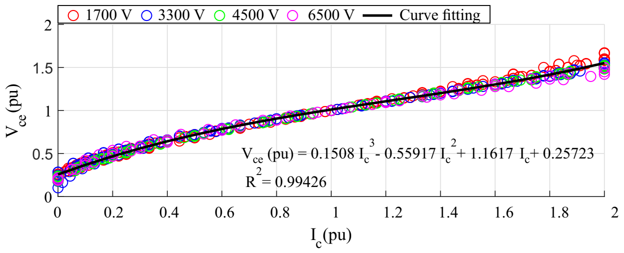

FIGURE 21. Curve fitting of typical IGBT conduction losses for 125°C in pu values.

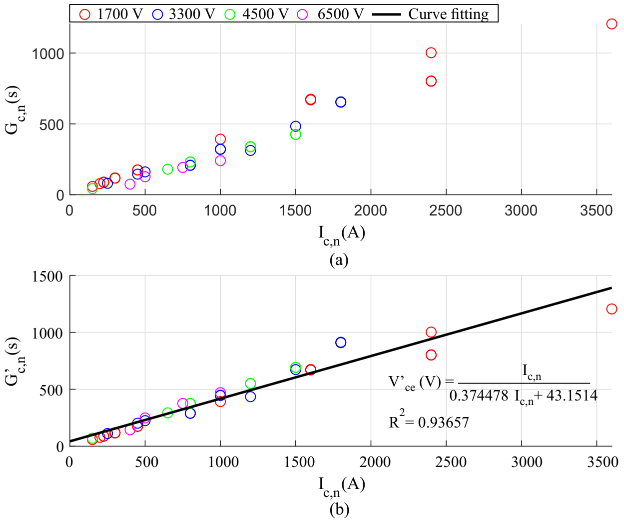

FIGURE 22. Typical IGBT conduction losses for 125°C in nominal values: (a) without blocking voltage correction; (b) with blocking voltage correction and curve fitting.

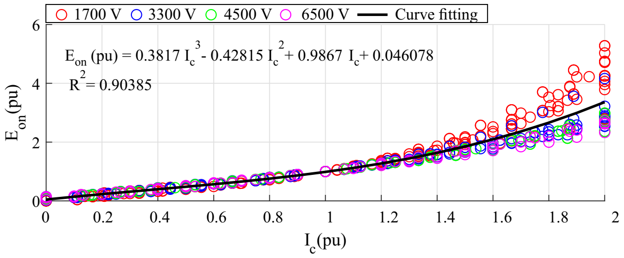

FIGURE 23. Curve fitting of typical IGBT turn-on energy for 125°C in pu values.

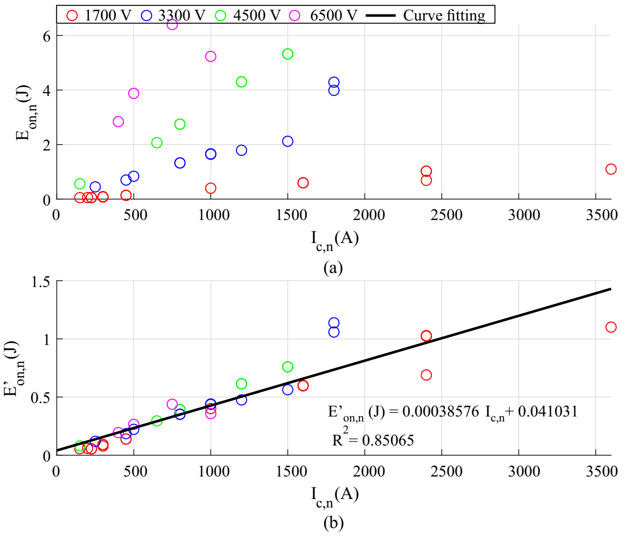

FIGURE 24. Typical IGBT turn-on energy for 125°C in nominal values: (a) without blocking voltage correction; (b) with blocking voltage correction and curve fitting.

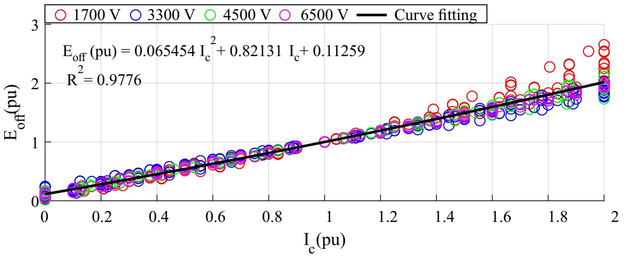

FIGURE 25. Curve fitting of typical IGBT turn-off energy for 125°C in pu values.

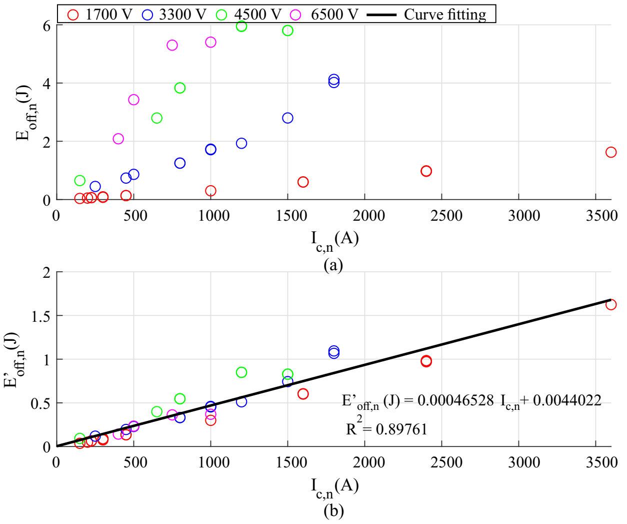

FIGURE 26. Typical IGBT turn-off energy for 125°C in nominal values: (a) without blocking voltage correction; (b) with blocking voltage correction and curve fitting.

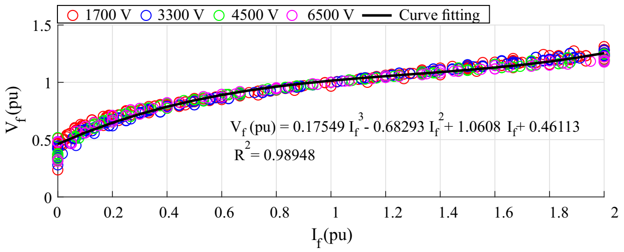

FIGURE 27. Curve fitting of typical diode conduction losses for 25°C in pu values.

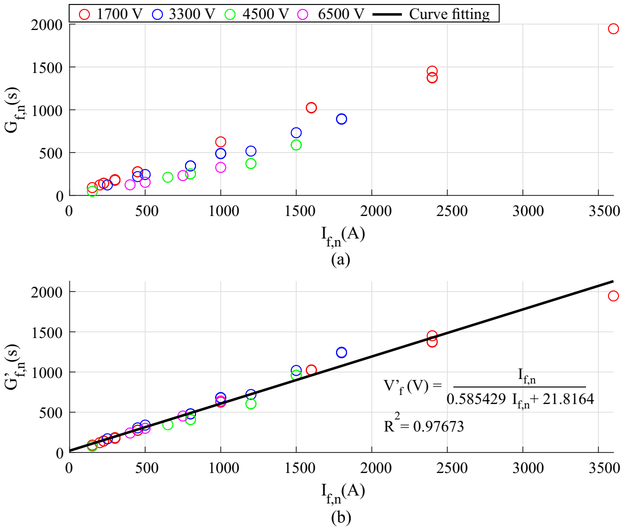

FIGURE 28. Typical diode conduction losses for 25°C in nominal values: (a) without blocking voltage correction; (b) with blocking voltage correction and curve fitting.

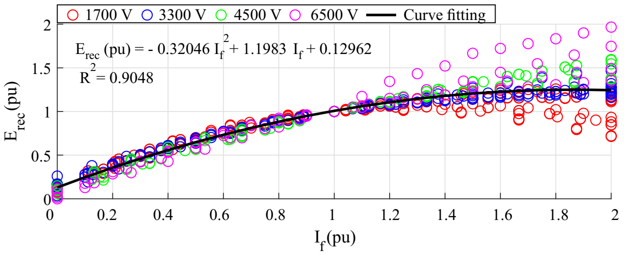

FIGURE 29. Curve fitting of typical diode reverse recovery energy for 25°C in pu values.

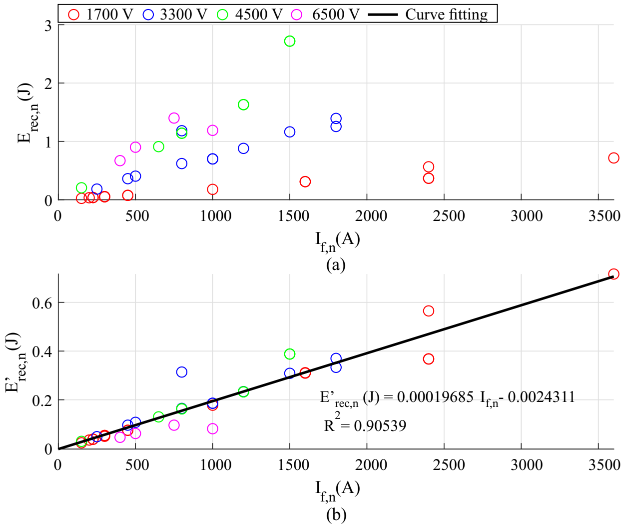

FIGURE 30. Typical diode reverse recovery energy for 25°C in nominal values: (a) without blocking voltage correction; (b) with blocking voltage correction and curve fitting.

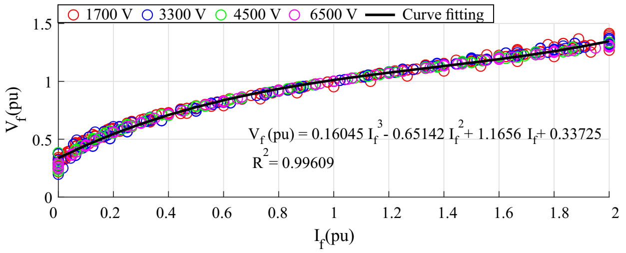

FIGURE 31. Curve fitting of typical diode conduction losses for 125°C in pu values.

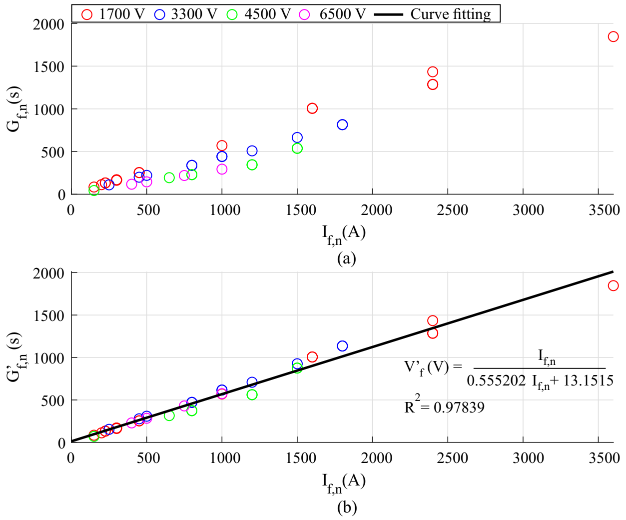

FIGURE 32. Typical diode conduction losses for 125°C in nominal values: (a) without blocking voltage correction; (b) with blocking voltage correction and curve fitting.

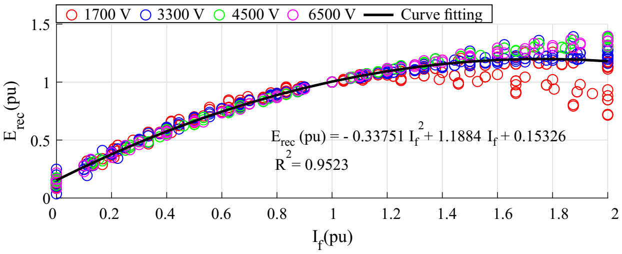

FIGURE 33. Curve fitting of typical diode reverse recovery energy for 125°C in pu values.

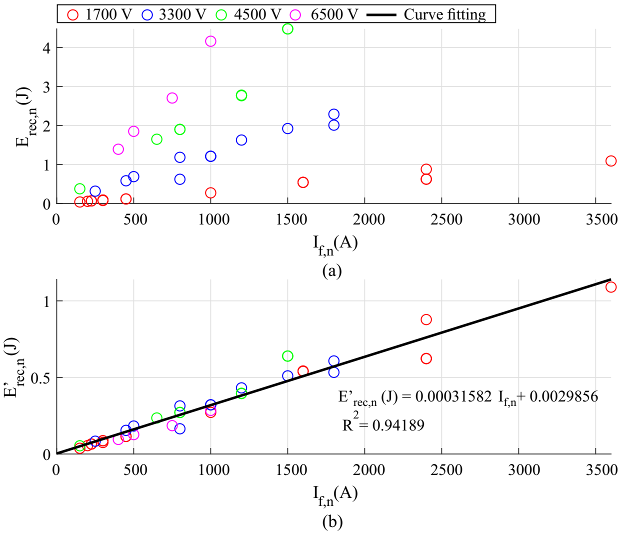

FIGURE 34. Typical diode reverse recovery energy for 125°C in nominal values: (a) without blocking voltage correction; (b) with blocking voltage correction and curve fitting.

B. Curve fitting for the IGBT and diode thermal resistances

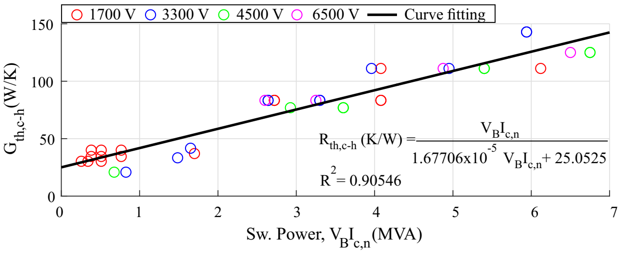

FIGURE 35. Curve fitting of typical IGBT case-heatsink thermal resistance.

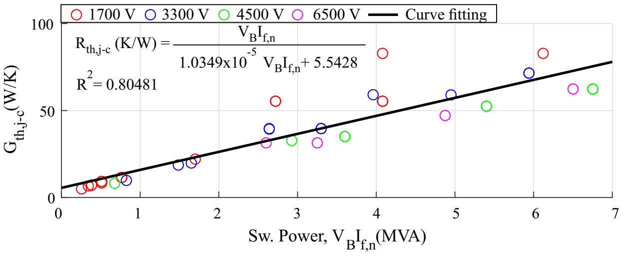

FIGURE 36. Curve fitting of typical diode junction-to-case thermal resistance.

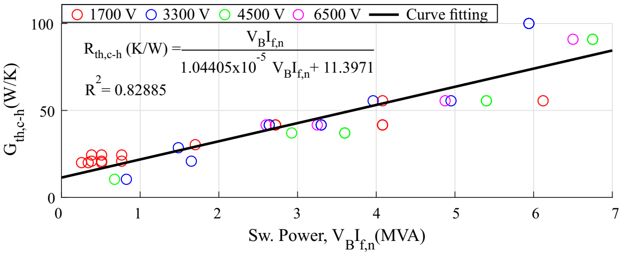

FIGURE 37. Curve fitting of typical diode case-heatsink thermal resistance.

C. Curve fitting for the diode silicon area

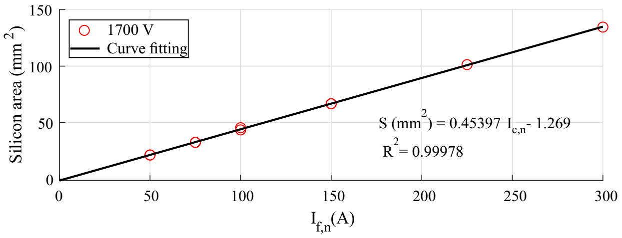

FIGURE 38. Curve fitting of typical silicon area for diode.

D. ABB modules and dies of the 1700 V blocking voltage considered in this work

TABLE 2. ABB modules (IGBT+diode) of 1700 V blocking voltage [18].

Part number Nom. current	Technology	
5SNG 0150Q170300	150 A	62Pak
5SNG 0200Q170300	200 A	62Pak
5SNG 0300Q170300	300 A	62Pak
5SNG 0225R170300	225 A	LoPak1
5SNG 0225R170390	225 A	LoPak1
5SNG 0300R170300	300 A	LoPak1
5SNG 0300R170390	300 A	LoPak1
5SNG 0450R170300	450 A	LoPak1
5SNG 0450R170390	450 A	LoPak1
5SNG 1000X170300	1000 A	LinPak
5SNA 1600N170300	1600 A	HiPak
5SNE 1600E170300	1600 A	HiPak
5SNA 2400E170305	2400 A	HiPak
5SNA 2400N170300	2400 A	HiPak
5SNE 2400E170300	2400 A	HiPak
5SNA 3600E170300	3600 A	HiPak

TABLE 3. ABB modules (IGBT+diode) of 3300 V blocking voltage [18].

Part number	Nom. current	Technology
5SNG 0250P330305	250 A	HiPak
5SNG 0450X330300	450 A	LinPak
5SND 0500N330300	500 A	HiPak
5SNA 0800N330100	800 A	HiPak
5SNE 0800E330100	800 A	HiPak
5SNA 1000N330300	1000 A	HiPak
5SNE 1000E330300	1000 A	HiPak
5SNA 1200E330100	1200 A	HiPak
5SNA 1200G330100	1200 A	HiPak
5SNA 1500E330305	1500 A	HiPak
5SNA 1800E330400	1800 A	HiPak
5SNA 1800G330400	1800 A	HiPak

TABLE 4. ABB modules (IGBT+diode) of 4500 V blocking voltage [18].

Part number	Nom. current	Technology
5SNG 0150P450300	150 A	HiPak
5SNA 0650J450300	650 A	HiPak
5SNA 0800J450300	800 A	HiPak
5SNE 0800G450300	800 A	HiPak
5SNA 1200G450300	1200 A	HiPak
5SNA 1200G450350	1200 A	HiPak
5SNA 1500G450300	1500 A	HiPak
5SNA 1500G450350	1500 A	HiPak

TABLE 5. ABB modules (IGBT+diode) of 6500 V blocking voltage [18].

Part number	Nom. current	Technology
5SNA 0400J650100	400 A	HiPak
5SNA 0500J650300	500 A	HiPak
5SNA 0600G650100	600 A	HiPak
5SNA 0750G650300	750 A	HiPak
5SNA 1000G650300	1000 A	HiPak

TABLE 6. ABB IGBT dies of the 1700 V blocking [19].

Part number	Nominal current	Technology
5SMY 86G1721	50 A	SPT+
5SMY 86J1722	75 A	SPT+
5SMY 86J1732	75 A	SPT++
5SMY 86K1722	100 A	SPT+
5SMY 86K1732	100 A	SPT++
5SMY 86L1731	120 A	SPT++
5SMY 86M1721	150 A	SPT+
5SMY 86M1730	150 A	SPT++
5SMY 86M1731	160 A	SPT++
5SMY 86P1730	225 A	SPT++

TABLE 7. ABB diode dies of the 1700 V blocking voltage [19].

Part number	Nominal current	Technology
5SLY 86E1700	50 A	SPT+
5SLZ 86E1700	50 A	SPT++/FSA
5SLY 86F1700	75 A	SPT+
5SLZ 86F1700	75 A	SPT++/FSA
5SLY 86G1700	100 A	SPT+
5SLZ 86G1700	100 A	SPT++/FSA
5SLY 86J1700	150 A	SPT+
5SLZ 86J1700	150 A	SPT++/FSA
5SLZ 86L1700	225 A	SPT++/FSA
5SLY 86M1700	300 A	SPT+

ACKNOWLEDGMENT

The authors are grateful for the financial support provided by the P&D project ANEEL/CEMIG D0727, CNPq (Conselho Nacional de Desenvolvimento Científico e Tecnológico) - projects 311056/2020-2, 408059/2021-4 and 307172/2022-8 and FAPEMIG (Fundação de Amparo à Pesquisa do Estado de Minas Gerais) - projects APQ-02556-21 and RED-00216-23. In addition, this work was carried out with the support of the CAPES (Coordenação de Aperfeiçoamento de Pessoal de Nível Superior) - Financing Code 001 and Academic Excellence Program (PROEX).

AUTHOR CONTRIBUTIONS

MENDONÇA, D.C.: Conceptualization, Formal Analysis, Investigation, Software, Validation, Visualization, Writing – Original Draft. **FRANÇA, J.V.G.**: Data Curation, Validation, Visualization, Writing – Review & Editing. **PEREIRA, H.A.**: Data Curation, Funding Acquisition, Resources, Writing – Review & Editing. **SELEME JR., S.I.**: Data Curation, Project Administration, Supervision, Writing – Review & Editing. **CUPERTINO, A.F.**: Conceptualization, Data Curation, Funding Acquisition, Methodology, Resources, Supervision, Writing – Review & Editing.

PLAGIARISM POLICY

This article was submitted to the similarity system provided by Crossref and powered by iThenticate – Similarity Check.

REFERENCES

[1] ABB, *Static compensator (STATCOM)*, URL: https://new.abb.com/facts/statcom.

[2] Siemens, *Optimal dynamic grid stabilization*, URL: https://www.siemens-energy.com/global/en/offerings/power-transmission/portfolio/flexible-ac-transmission-systems/svcplus.html.

[3] GE, *Static Synchronous Compensator (STATCOM) Solutions*, URL: https://www.gegridsolutions.com/products/brochures/powerd_vtf/STATCOM_GEA31986_HR.pdf.

[4] M. Hagiwara, R. Maeda, H. Akagi, "Negative-Sequence Reactive-Power Control by a PWM STATCOM Based on a Modular Multilevel Cascade Converter (MMCC-SDBC)", *IEEE Transactions on Industry Applications*, vol. 48, no. 2, pp. 720–729, March-April 2012, doi:10.1109/TIA.2011.2182330.

[5] O. Oghorada, L. Zhang, "Analysis of star and delta connected modular multilevel cascaded converter-based STATCOM for load unbalanced compensation", *International Journal of Electrical*

Power & Energy Systems, vol. 95, pp. 341–352, February 2018, doi:10.1016/j.ijepes.2017.08.034.

[6] D. d. C. Mendonça, J. M. S. Callegari, A. F. Cupertino, H. A. Pereira, S. I. Seleme Júnior, "Delta-CHB Statcom with Reduced Capacitance Through Third Harmonic Injection", *Eletrônica de Potência*, , no. 2, p. 151–162, May 2023, doi:10.18618/REP.2023.2.0052.

[7] T. Friedli, J. W. Kolar, "A Semiconductor Area Based Assessment of AC Motor Drive Converter Topologies", *in 2009 Twenty-Fourth Annual IEEE Applied Power Electronics Conference and Exposition*, pp. 336–342, February 2009, doi:10.1109/APEC.2009.4802678.

[8] J. E. Huber, J. W. Kolar, "Optimum Number of Cascaded Cells for High-Power Medium-Voltage AC–DC Converters", *IEEE Journal of Emerging Selected Topics in Power Electronics*, vol. 5, no. 1, pp. 213–232, March 2017, doi:10.1109/JESTPE.2016.2605702.

[9] D. Do Carmo Mendonça, J. V. G. Franca, H. A. Pereira, S. I. S. Júnior, A. F. Cupertino, "Third Harmonic Circulating Current Injection Effects on Optimum Silicon Area of Delta-CHB STATCOM", *in 2023 IEEE 8th Southern Power Electronics Conference and 17th Brazilian Power Electronics Conference (SPEC/COBEP)*, pp. 1–8, November 2023, doi:10.1109/SPEC56436.2023.10408553.

[10] D. do Carmo Mendonça, A. Fagner Cupertino, H. Augusto Pereira, S. Isaac Seleme Júnior, R. Teodorescu, "Estratégia De Tolerância A Falhas Para Um Conversor Delta-Chb Statcom Na Região De Sobremodulacão", *Eletrônica de Potência*, vol. 25, no. 4, p. 395–404, December 2020, doi:10.18618/REP.2020.4.0029, URL: https://journal.sobraep.org.br/index.php/rep/article/view/293.

[11] J. V. G. França, J. H. D. G. Pinto, D. d. C. Mendonça, J. V. M. Farias, R. O. d. Sousa, H. A. Pereira, S. I. Seleme Júnior, A. F. Cupertino, "Development of a Didactic Platform for Flexible Power Electronic Converters", *Eletrônica de Potência*, vol. 27, no. 3, p. 225–235, August 2022, doi:10.18618/REP.2022.3.0012, URL: https://journal.sobraep.org.br/index.php/rep/article/view/73.

[12] F. Beltrame, F. H. Dupont, H. C. Sartori, E. C. Cancian, L. Roggia, J. R. Pinheiro, "Design of Boost Converter Based on Optimum Weighted Average Efficiency for Photovoltaic Systems", *Eletrônica de Potência*, vol. 19, no. 3, p. 295–302, August 2014, doi:10.18618/REP.2014.3.295302, URL: https://journal.sobraep.org.br/index.php/rep/article/view/505.

[13] P. Roberto Matias Junior, J. V. Matos Farias, A. Fagner Cupertino, G. Alves Mendonça, M. Martins Stopa, H. Augusto Pereira, "Seleção Da Tensão De Bloqueio Ótima De Igbts Para Inversores De Frequência Baseados Em Conversor Modular Multinível", *Eletrônica de Potência*, vol. 25, no. 4, p. 405–414, December 2020, doi:10.18618/REP.2020.4.0033, URL: https://journal.sobraep.org.br/index.php/rep/article/view/294.

[14] B. J. Baliga, *The IGBT Device*, Elsevier, 2015, doi:10.1016/C2012-0-02174-6.

[15] K. Ma, A. S. Bahman, S. Beczkowski, F. Blaabjerg, "Complete Loss and Thermal Model of Power Semiconductors Including Device Rating Information", *IEEE Transactions on Power Electronics*, vol. 30, no. 5, pp. 2556–2569, May 2015, doi:10.1109/TPEL.2014.2352341.

[16] A. Marzoughi, R. Burgos, D. Boroyevich, Y. Xue, "Design and Comparison of Cascaded H-Bridge, Modular Multilevel Converter, and 5-L Active Neutral Point Clamped Topologies for Motor Drive Applications", *IEEE Transactions on Industry Applications*, vol. 54, no. 2, pp. 1404–1413, March-April 2018, doi:10.1109/TIA.2017.2767538.

[17] M. Schweizer, I. Lizama, T. Friedli, J. W. Kolar, "Comparison of the chip area usage of 2-level and 3-level voltage source converter topologies", *in IECON 2010 - 36th Annual Conference on IEEE Industrial Electronics Society*, pp. 391–396, November 2010, doi:10.1109/IECON.2010.5674994.

[18] H. Energy, *Insulated Gate Bipolar Transistor (IGBT) and diode modules with SPT, SPT+, SPT++ and TSPT+ chips*, URL: https://www.hitachienergy.com/products-and-solutions/semiconductors/insulated-gate-bipolar-transistor-igbt-and-diode-modules.

[19] H. Energy, *Insulated-gate bipolar transistors (IGBT) and diode dies*, URL: https://www.hitachienergy.com/products-and-solutions/semiconductors/insulated-gate-bipolar-transistors-igbt-and-diode-dies.

BIOGRAPHIES

Dayane do Carmo Mendonça graduated in Electrical Engineering from the Federal University of Viçosa (UFV) in 2019. In April 2021, she was granted a Master's degree in Electrical Engineering from the Graduate Program in Electrical Engineering at CEFET-MG/UFSJ. She is currently a doctoral student at the Graduate Program in Electrical Engineering at the Federal University of Minas Gerais (UFMG) and a specialist at the Gerência de Especialistas em Sistemas Elétricos de Potência (GESEP-UFV). Her main research interests include modular multilevel converters and renewable energy generation systems.

João Victor Guimarães França graduated in Electrical Engineering from the Federal University of Viçosa (UFV) in 2022. In February 2024, he was granted a Master's degree in Electrical Engineering from the Graduate Program in Electrical Engineering at CEFET-MG/UFSJ. He is currently a doctoral student at the Graduate Program in Electrical Engineering at CEFET-MG/UFSJ and a specialist at the Gerência de Especialistas em Sistemas Elétricos de Potência (GESEP-UFV). His main research interests include modular multilevel converters, focused on the Delta-CHB topology for STATCOM realization.

Heverton Augusto Pereira received the B.S. degree from the Federal Federal University of Viçosa (UFV), Viçosa, Brazil, in 2007, the M.Sc. degree from the University of Campinas, Campinas, Brazil, in 2009, and the Ph.D. degree from the Federal University of MinasGerais, Belo Horizonte, Brazil, in 2015, all of then in Electrical Engineering. He was a visiting Researcher from the Department of Energy Technology, Aalborg University, Denmark, in 2014. He worked as an Adjunct Professor with the Electric Engineering Department, UFV, since 2009. His main research interests include grid-connected converters for PV and wind power systems and high-voltage dc/flexible ac transmission systems based on MMC.

Seleme Isaac Seleme Júnior holds a degree in Electrical Engineering from the University of São Paulo (1977), a Master's degree in Electrical Engineering from the Federal University of Santa Catarina (1985), and a PhD in AutomatiqueProdutique - Institut National Polytechnique de Grenoble(1994). He took postdocs at the Power Electronics Group at U. C. Berkeley (2002) and at the University of Toulouse, at the LAPLACE Laboratory (2015/16) with a CAPES grant. He is currently a professor at the Federal University of Minas Gerais, with experience in Electrical Engineering and emphasis on Electronic Process Control, Feedback. His activities involve induction motor, electric drives, energy minimization, non-linear control in power electronic converters with application in renewable energy sources and control of electronic ballasts. More recently, as a result of the 2015/16 post-doctorate, he has been working with multilevel converters, coordinating a CAPES-COFECUB cooperation project and supervising doctoral and master's programs on the subject.

Allan Fagner Cupertino received the B.S. degree in electrical engineering from the Federal University of Viçosa (UFV) in 2013, the M.S. and Ph.D. degrees in Electrical Engineering from the Federal University of Minas Gerais (UFMG) in 2015 and 2019, respectively. He was a guest Ph.D. at the Department of Energy Technology, Aalborg University from 2018 to 2019. From 2014 to 2022, he was an Assistant Professor in the area of electric machines and power electronics at the Federal Center of Technological Education of Minas Gerais (CEFET). Since 2023, he has been with the Department of Electrical Energy at the Federal University of Juiz de Fora (UFJF). His main research interests include renewable energy conversion systems, smart battery energy storage systems, cascaded multilevel converters, and reliability of power electronics. Prof. Cupertino was the recipient of the President Bernardes Silver Medal in 2013, the SOBRAEP Ph.D. Thesis Award in 2020 and the IAS CMD Ph.D. Thesis Contest in 2021. He is a member of the Brazilian Power Electronics Society (SOBRAEP) and Brazilian Society of Automatics (SBA).